Analysis of Ballistic Anomalies in Solid Rocket Motors

S. D. Heister* and E. M. Landsbaum†
The Aerospace Corporation, Los Angeles, California 90009

Ballistic anomalies, defined as pressure deviations from the normally expected trace, have occurred frequently during solid rocket motor firings. This paper describes techniques for determining the probable cause of such anomalies. Mass and energy balance relationships, which account for changes in chamber volume and throat area, are derived for the purpose of calculating a burning surface history that corresponds to pressure data from flight measurements or static tests. Results indicate that chamber temperature variations caused by ballistic anomalies are negligible. Characteristic burning surface signatures for propellant voids, cracks, unbonds, and high burn rate pockets are discussed. Conservation of momentum relationships are derived for the purpose of describing anomalies caused by mass ejection through the nozzle throat. Specific examples form inertial upper stage motors and the Titan T34-D solid rocket booster are presented to illustrate the application of the generic analysis techniques described in this paper.

Nomenclature

A_b = burning surface area
A_t = throat area
C_{fv} = thrust coefficient
C_p = specific heat at constant pressure
C_v = specific heat at constant volume
c = pre-exponential constant in burning rate law
c^* = characteristic velocity
F = thrust
f = nondimensional thrust, F/F_o
g = acceleration due to gravity
k_b = nondimensional burning surface area, A_b/A_{bo}
k_t = nondimensional throat area, A_t/A_{to}
M = molecular weight of chamber gases
n = burning rate exponent
P = pressure
p = nondimensional pressure, P/P_o
R = universal gas constant
r = propellant burn rate
T = temperature
T_f = flame temperature
t = time
V = chamber volume
w = flow rate
x = debond length
α = crack or debond angle (see Figs. 5 and 6)
γ = ratio of specific heats
ΔA_b = additional burn surface above that normally expected
ρ_g = gas density
ρ_{go} = gas density assuming flame temperature, PM/RT_f
ρ_s = propellant density
τ = motor time constant, $P_oMV_o/RT_f\dot{w}_o$

Subscript

o = equilibrium condition

Introduction

BALLISTIC anomalies in solid rocket motors (SRM) range from very small pressure disturbances, sometimes referred to as "blips," to disturbances that may generate a chamber pressure twice the normal value. A given anomaly can affect the chamber pressure for periods of time ranging from a few milliseconds to tens of seconds. The three primary causes for ballistic anomalies include: 1) unexpected increase in burning surface area, 2) mass ejection, and 3) high burn rate pockets.

Analysis of ballistic anomalies that occur during motor tests is important because design deficiencies may be uncovered through such an analysis. For instance, an anomaly that appears as a small disturbance on ground test may appear as a much larger disturbance in flight due to increased acceleration loads on the motor. Signatures characteristic of propellant debonds should be of concern because increased heat transfer behind the debond could result in excessive insulation erosion and a possible case failure. Signatures consistent with mass ejection could signal the loss of an igniter or restrictor insulation.

This paper discusses the characteristics of each of the three major causes of anomalies. Specific examples from inertial upper stage (IUS) motors and Titan T34-D solid rocket boosters (SRB) are included to illustrate results of the analyses. Different equations are derived to analyze the different classes of anomalies. All equations assume that the gas properties are constant throughout the chamber volume. The authors believe this to be a satisfactory assumption since, in most cases, the wave travel time within the chambers will be small compared to the time involved in the anomaly. There will be cases where the analyst may want to consider a full transient analysis of the motor chamber. However, it is likely that the instrumentation accuracy is inadequate to warrant this more sophisticated approach. Thus, the equations presented should be adequate for essentially all anomaly studies.

Increase in Burn Area

An unexpected increase in burning surface area is probably the most common cause for ballistic anomalies. This anomaly manifests itself because of propellant cracks or debonds that arise from stresses within the grain. One calculates the difference in burn area between the anomalous and normal case from the pressure perturbation. The unsteady terms must be considered. Then from a grain geometry analysis, one estimates the most likely cause of the anomaly.

The equations expressing the conservation of mass and energy within the rocket motor can be written as follows:

Mass balance:

$$r\rho_s A_b - \frac{gPA_t}{c_o^*\sqrt{T/T_f}} = \frac{\mathrm{d}}{\mathrm{d}t}\left(\frac{PMV}{RT}\right) \tag{1}$$

Received Dec. 8, 1985; revision received July 18, 1989.

*Member of the Technical Staff, P.O. Box 92957.
†Engineering Specialist, P.O. Box 92957, Mail Station M4/969. Member AIAA.

Energy balance:

$$r\rho_s A_b C_p T_f - \frac{gPA_t C_p T}{c_o^* \sqrt{T/T_f}} = \frac{\mathrm{d}}{\mathrm{d}t}\left(\frac{PMVC_v}{R}\right) \tag{2}$$

The derivation assumes ideal gases and that specific heats, flame temperature, and molecular weight are all constant.

Equation (1) can be solved for the burning surface by substituting cP^n for the propellant burn rate and rA_b for the volume derivative with respect to time. Use of the steady-state form of the burning rate equation (cP^n) is adequate unless the disturbance is very large (see Ref. 1). The resulting equation becomes

$$A_b = \frac{\{(gPA_t/c_o^*\sqrt{T/T_f}) + \rho_g V[(\dot{P}/P) - (\dot{T}/T)]\}}{cP^n(\rho_s - \rho_g)} \tag{3}$$

where dotted quantities represent derivatives with respect to time. Substituting Eq. (3) into Eq. (2) and solving for the temperature derivative gives

$$\dot{T} = \frac{gPA_t\sqrt{TT_f}}{\rho_g V c_o^*}\left(1 - \frac{T}{\lambda T_f}\right) + \frac{\dot{P}T}{P}\left(1 - \frac{T}{T_f\gamma\lambda}\right) \tag{4}$$

where $\lambda = (\rho_s - \rho_{go}/\gamma)/(\rho_s - \rho_g)$ and ρ_{go} corresponds to the gas density calculated using flame temperature. Since $\rho_s \gg \rho_g$ for solid propellants, the quantity λ is very close to 1.

Results indicate that temperature variations are negligible, although this conclusion is not obvious. The second half of Eq. (4) corresponds to the temperature change due to an adiabatic compression, but it is balanced by the first half of the equation. Numerical calculations show that the two halves essentially negate each other. The maximum temperature rise is obviously the adiabatic value. If one assumes that all variables on the right side of Eq. (4) except temperature are constant, the temperature rise can be shown to be negligible by analysis. For this reason, temperature variation can be neglected and Eq. (3) becomes

$$A_b = \frac{gPA_t/c_o^* + \rho_{go}V(\dot{P}/P)}{cP^n(\rho_s - \rho_{go})} \tag{5}$$

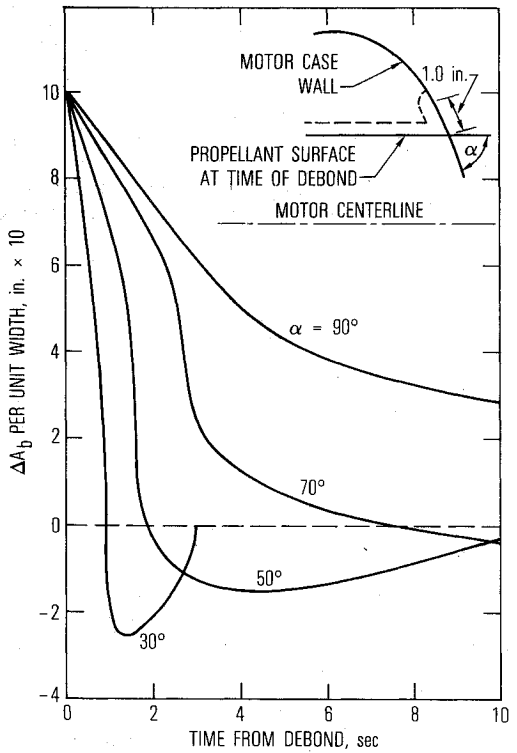

Fig. 1 Typical decay of a propellant debond.

Equation (5) can be used to solve for the burning surface history from the pressure history, as will be illustrated. Variations of c^* with pressure and A_t with time may also be incorporated.

Burn Area Changes Resulting from Cracks or Debonds

The calculation of the crack or unbond necessary to match the observed anomaly is more difficult than the estimation of the burn area change required. This is because area increases due to cracks or unbonds decay with time, which will be illustrated with two simple examples before presenting the analysis of the Titan anomaly.

The increase in burning area for a debond 1 in. deep and 10 in. in length is shown in Fig. 1. The time is based on a propellant burn rate of 0.3 in./s. The calculation is parameterized in terms of the angle between the propellant surface and the wall, and end effects are ignored. The decay times in Fig. 1 are much longer than those associated with a mass ejection (see Mass Ejection section).

Figure 2 presents the decay for an assumed crack 1 in. deep and 10 in. in length. Results are presented as a function of the angle α from the burn front. Note that cracks also decay slowly unless the angle becomes very small. The purpose of these illustrations is so the reader will recognize that the additional area produced by an unbond or crack decays with time. Cracks will decay and asymptote to zero ΔA_b. Unbonds will go through a negative ΔA_b before returning to zero.

Titan Unbond Calculation

To illustrate the method of anomaly analysis presented in the previous sections, a pressure disturbance encountered on a recent Titan T34D flight will be considered. The Titan launch vehicle is equipped with two stage zero SRBs that are 70 ft in length and carry about 464,000 lb of propellant each. Figure 3 provides a schematic of a T34D SRB. Figures 4 and 5 present the pressure history and an expanded pressure history during

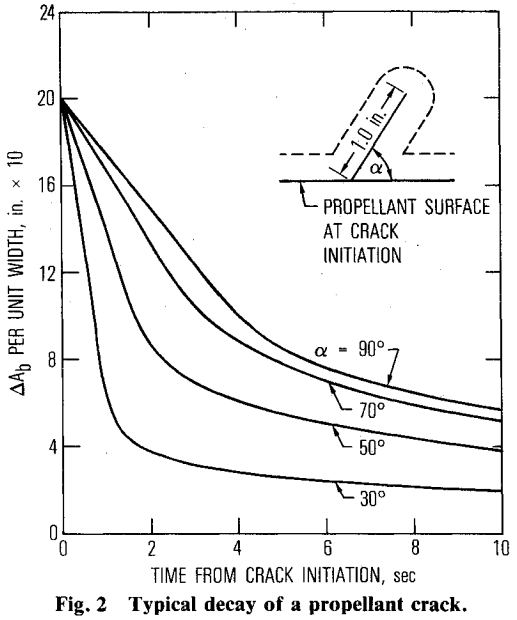

Fig. 2 Typical decay of a propellant crack.

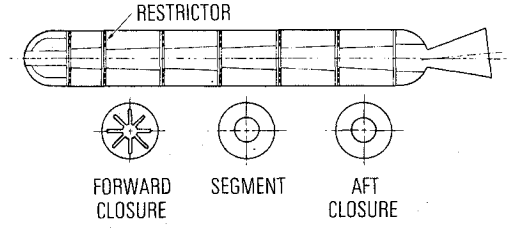

Fig. 3 Titan T34D solid rocket booster schematic.

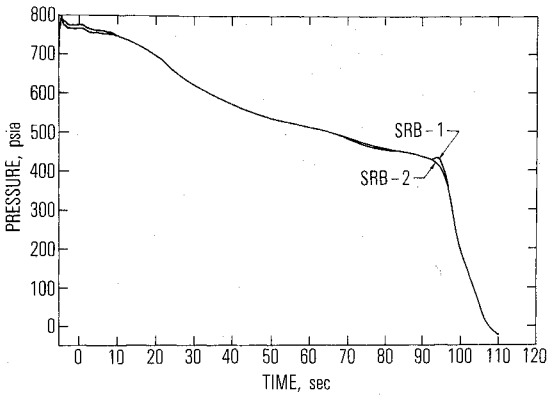

Fig. 4 T34D measured chamber pressure history.

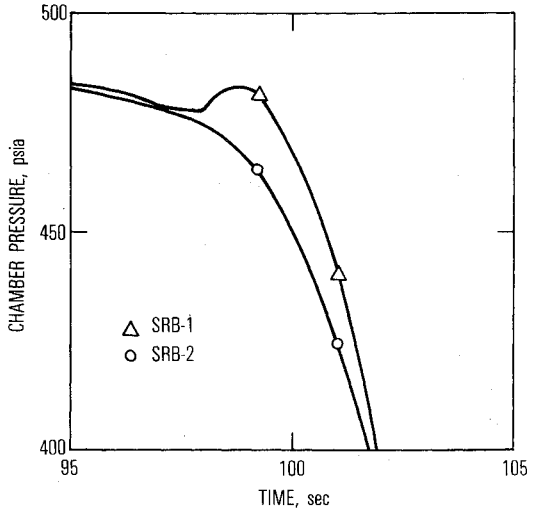

Fig. 5 Chamber pressure during disturbance.

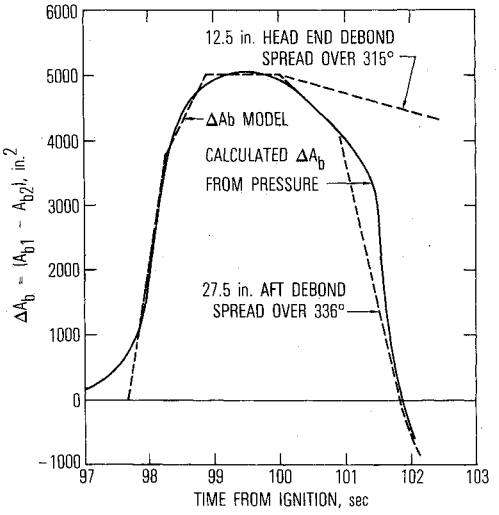

Fig. 6 Additional burn surface required to generate disturbance.

the disturbance for each of the two SRBs. Since the pressure disturbance has such a long rise time (1 s), mass ejection was ruled out immediately (see Mass Ejection section) and a propellant debond was investigated.

Since the disturbance occurred during tailoff, it is difficult to determine what the pressure history might have been had the disturbance not occurred. For this reason, SRB-2 was used as the normal pressure trace for comparative purposes. Equation (5) can be used to solve for the burning surface area for

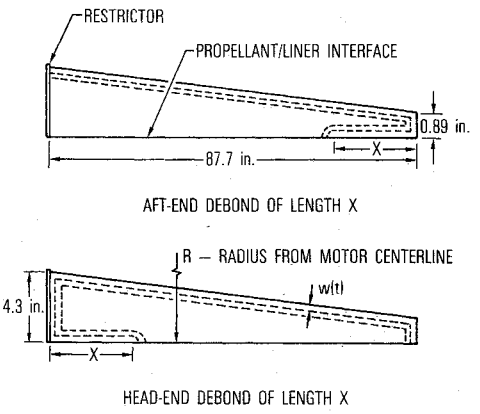

Fig. 7 Segment geometry.

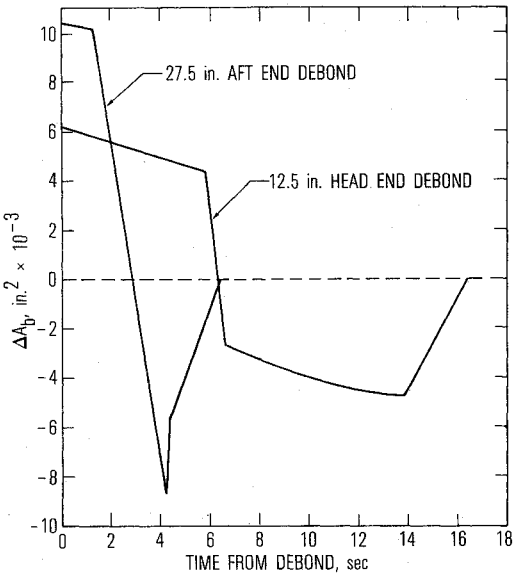

Fig. 8 Debond decay.

both the anomalous pressure history and normal pressure history. By taking the difference of the two calculations, one can obtain the ΔA_b that would cause the disturbance as a function time. The resulting ΔA_b calculation is shown as the solid line in Fig. 6.

Each SRB contains 5½ segments, a forward closure, and an aft closure (Fig. 3). Both the forward and aft closures have burned out by 97 s, and the segment geometry at this time is shown in Fig. 7 along with illustrations of both head- and aft-end segment debonds. From the segment geometry and the propellant burn rate, one can calculate the resulting ΔA_b time history for either a head- or aft-end debond and for different debond lengths x and circumferential angles. Figure 8 presents results of calculations assuming a 360-deg debond in either the head or aft end of the segment. The analysis shows the aft-end debonds decay much more rapidly than head-end debonds.

The matching of the physical unbond propagation to that derived from the pressure anomaly (Fig. 6) is a trial and error process. One might expect most unbonds to propagate outward in an irregular manner. This propagation is very difficult to examine theoretically. The authors have assumed a finite-length unbond that propagates circumferentially. A minimum length can be determined since the propagation is limited to 360 deg. The selected unbond propagation is shown in Fig. 9. This propagation was selected to match an idealized unbond model represented by the line segments in Fig. 6. Unbond length is not a strong influence in the vicinity of the selected value. The debond only propagates until the maximum ΔA_b area is matched. After that, each unbond has its own unique

decay. Even though the unbond area is increasing, at the end, the resulting ΔA_b is constant at 5000 in.^{2}, represented by the horizontal line of Fig. 6. The total unbonded area is 9660 in.^{2} for the aft unbond and 5480 in.^{2} for the forward unbond.

Although Fig. 6 seems to show that an aft-end debond is more likely, the effects on chamber pressure are less pronounced. The pressure history resulting from a forward- or aft-end debond is shown in Fig. 10. Since the ΔA_b calculated from the pressure resulted from the assumption that the SRB-2 pressure represented a nondisturbed pressure for SRB-1, the differences in pressure for forward- and aft-end debonds are not conclusive. The authors believe a forward-end debond is more likely due to stresses induced by the forward restrictor. However, the results of the analysis suggest stronger consideration for side-wall or aft-end unbonds.

Another factor obscuring the conclusions is the simplicity of the debond model used. Although the assumption of circumferential propagation is probably not valid, results from this assumption are easily calculable and provide insight into the depth and amount of propagation required to fit the pressure data. More realistic models would consider additional axial propagation or a semicircular debond growing in radius, but these models present greater difficulties in calculating the resulting ΔA_b histories.

Mass Ejection

For the purpose of this paper, the term mass ejection will represent the discharge of an inert body through the nozzle throat. As an inert body enters the throat region, the flow blockage causes an increase in chamber pressure and a decrease in thrust. For chambers with a small L^* value or for port-to-throat ratios approaching unity, an increase in thrust could be observed; for most rocket motors, a decrease will be observed.

Numerical computations involving bodies up to 8 in. in length and weighing up to 12.6 lb show that ejected masses block the throat for times < 10 ms (see Ref. 2). Therefore, anomalies in which the pressure rises over a very short time will be characteristic of mass ejections, while anomalies associated with increased burn surface will generally have longer rise times. A long rise time could be obtained by having a small blockage for a long time, but this condition is very unlikely. After the body leaves the throat, the thrust will rapidly rise to the value associated with the higher chamber pressure and the momentum of the body and will then decay to the steady-state value. A similar decay in chamber pressure will be noted after the body leaves the throat region.

Blockage and Pressure Decay Calculations

The magnitude of the maximum and minimum thrust during the perturbation, as well as the thrust and pressure decay, can be obtained by using a quasisteady solution to the mass balance equation. Strictly speaking, a full transient analysis of the chamber and nozzle could be done (as in Ref. 2) to analyze the short times of nozzle blockages because the blockage time will be small compared to the motor time constant. However, this approach requires a trial and error process of selected blockages (using an idealized case) and calculating the expected pressure measurement response. Considering the difficulties of two-dimensional transient subsonic flow and the probable inaccuracy of the original instrumentation, this approach does not appear generally worthwhile. The simpler analysis to be presented would be used to generate initial blockage estimates for any full transient analysis and should be satisfactory for most blockage evaluations.

The mass balance equation is solved assuming step changes in throat area, and the decay is calculated by removing the perturbation. Gas temperature changes can be ignored for the same reasons previously discussed. The propellant burn rate lags the pressure perturbation by < 10 ms (see Ref. 3). Assuming steady-state burning prior to the perturbation and a burning rate law of cP^n gives the equilibrium mass flow at time zero prior to the disturbance

$$\dot{w}_o = cP^n(\rho_s - \rho_{go})A_{bo} = gP_oA_{to}/c^* \tag{6}$$

where the characteristic velocity is assumed to be constant ($c^* = c_o^*$).

Rearranging Eq. (5), assuming constant volume, and dividing by Eq. (6) gives the nondimensional form of the mass balance equation

$$k_bp^n - k_tp = \tau\dot{p} \tag{7}$$

where k_b and k_t are the nondimensional burn surface and throat areas, respectively. In this case, k_t represents the ratio of the blocked throat area to the initial unblocked throat area. The time constant $\tau = (P_oMV_o)/(RT_f\dot{w}_o)$ represents the time to exhaust the gas from the chamber at the equilibrium flow rate. Motor time constants typically vary between 0.01 s for small chambers to 0.5 s for very large chambers. The assumption of constant volume is accurate unless the quantity $\dot{V}t/V_o$

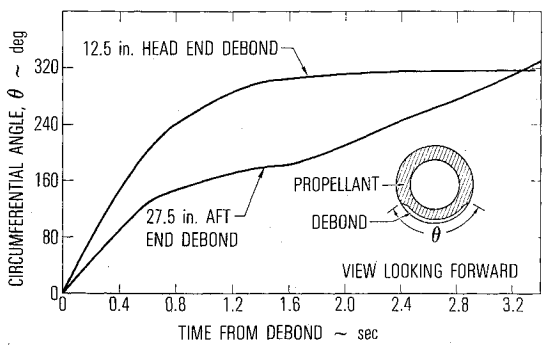

Fig. 9 Propagation histories for forward and aft debonds.

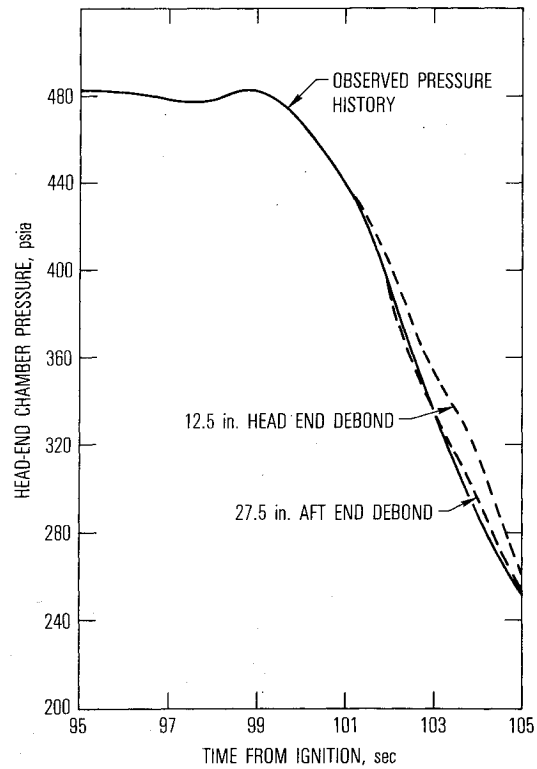

Fig. 10 Calculation pressure history for head- and aft-end debonds.

is not small compared to unity. The p in Eq. (7) corresponds to the P/P_o from test data because P_o in a test reflects the effects of increasing chamber volume. Assuming that both k_b and k_t are constant, the well-known integration of Eq. (7) is

$$p = \left\{\frac{k_b}{k_t} - \frac{k_b - k_t}{k_t}\left[\exp - k_t(1-n)\frac{t}{\tau}\right]\right\}^{1/(1-n)} \tag{8}$$

where t is measured from the start of the disturbance. Equation (8) gives the magnitude of pressure rise corresponding to a step change in burn surface or throat area. Since we are considering a blockage that occurs over the period of a few milliseconds, k_b can be assumed to be unity and Eq. (8) can be used to calculate the average blockage k_t necessary to generate the disturbance.

The theoretical decay can be calculated using Eq. (9), assuming that the burn surface is equal to the steady-state value and the blockage disappears instantaneously

$$t - t_1 = \frac{\tau}{(1-n)} \ln \frac{p_1^{1-n} - 1}{p^{1-n} - 1} \tag{9}$$

where at t_1 the pressure perturbation is p_1. If the event occurs when the burn area is changing rapidly, Eq. (9) is not valid and Eq. (7) must be integrated numerically to obtain an accurate result.

Thrust Calculations

If there is no throat blockage, the thrust increase is directly related to the pressure increase

$$F = C_{fv} P A_t \tag{10}$$

where C_{fv} is the motor thrust coefficient. Dividing Eq. (10) by the thrust prior to the disturbance

$$F_o = C_{fvo} P_o A_{to} \tag{11}$$

gives

$$f = p \tag{12}$$

since C_{fv} is a very weak function of pressure. If there is throat blockage, then

$$F = C_{fv} P A_{to} k_t + P A_{to}(1 - k_t) \tag{13}$$

The first term is the normal calculation of thrust. The nozzle stay time is less than the perturbation times; therefore, the assumption that the pressure distribution in the nozzle is that for the chamber pressure under steady-state conditions is reasonable. There is a slight error because the pressure integral over the exit cone with an annular nozzle throat will be slightly different than that for a normal circular throat. The second term results from the change in momentum of the body. Results in Ref. 2 indicate that the force on the body in the throat region can be closely approximated by simply taking the product of the chamber pressure and the body cross-sectional area. This approximation slightly overpredicts the body force because the back pressure on the body is never zero.

Dividing both side of Eq. (13) by Eq. (11) gives

$$f = p\left[\frac{C_{fv}}{C_{fvo}} k_t + \frac{(1 - k_t)}{C_{fvo}}\right] \tag{14}$$

where C_{fv} is the thrust coefficient for the larger expansion ration ($\epsilon = \epsilon_o / k_t$) associated with the partially blocked throat.

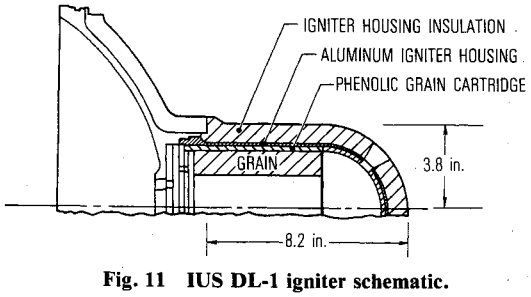

Fig. 11 IUS DL-1 igniter schematic.

IUS DL-1 Mass Ejection Analysis

A first stage IUS development motor fired in November 1979 provides an excellent example of a mass ejection event. The motor, which has a head-end igniter as depicted in Fig. 11, ejected the external igniter insulation at motor ignition. About 12.5 s after ignition, part of the aluminum on the aluminum housing began burning, and at 13.5 s, most of the remainder of the housing and internal insulation was ejected. Taking into account the amount of aluminum burned and the portions of the housing remaining after the firing gives an estimate of 6–7 lb for the ejected mass.

A plot of the chamber pressure and thrust during the ejection is presented in Figs. 12 and 13. The pressure plot represents the average of two transducers with 500 samples per second (sps), whereas the thrust is 100-sps data. Figure 12 shows a 16-psi rise in 6 ms, whereas 100-sps data showed a 9-psi rise in 10 ms. This comparison shows that high data rates are necessary to properly resolve the size of the disturbance. In fact, even the 500-sps data overestimate the rise time, and the peak pressure may result from transducer overshoot.

Since the disturbance occurred early in the firing, when the chamber volume was small, the time constant was relatively short (τ = 0.031 s). To compensate for transducer overshoot, the peak pressure for the decay calculation was estimated by averaging the measured peak and the first valley following the peak. This method gives a nondimensional pressure rise of 3.8%. For a burn rate exponent of 0.29, the decay curve can be calculated from Eq. (9). Results of this calculation (shown in Fig. 12) agree well with the data. Note that the total decay time is of the order of three time constants and is much less than those for either cracks or debonds (see previous section).

The calculated blockage is primarily a function of $\dot{P}$, therefore, transducer overshoot does not influence the calculation.

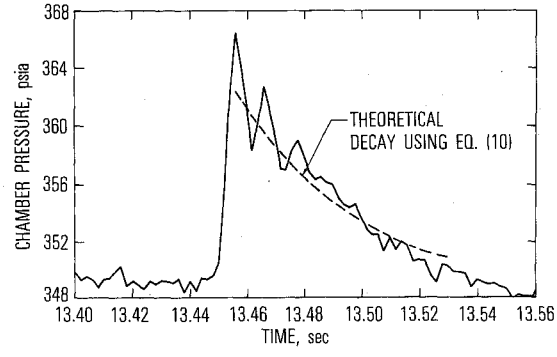

Fig. 12 Chamber pressure during mass ejection.

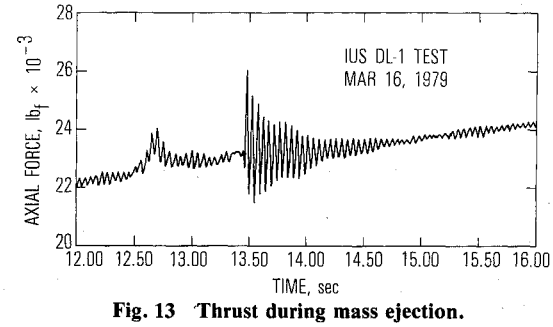

Fig. 13 Thrust during mass ejection.

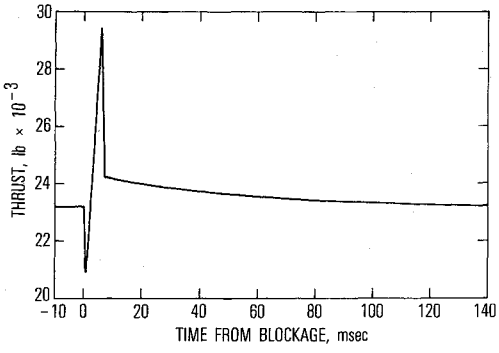

Fig. 14 Thrust model calculated from pressure data.

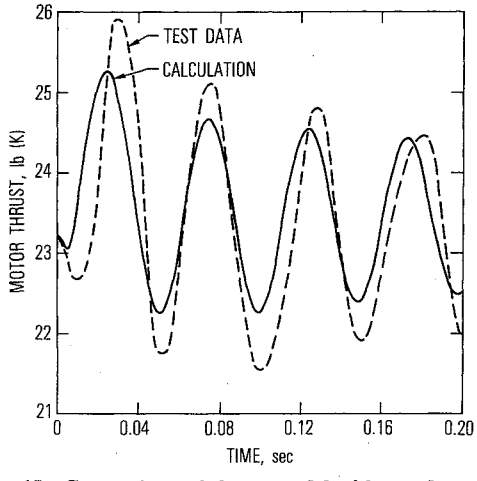

Fig. 15 Comparison of thrust model with test data.

Using a blockage time of 6 ms and a nondimensional pressure rise of 1.045, which corresponds to 16 psi, gives a k_t value calculated from Eq. (8) of 0.76. Using an unblocked expansion ratio of 58, a ratio of specific heats of 1.2, and a C_{fvo} of 1.82 gives a nondimensional blocked thrust of 0.90 by using Eq. (14).

To obtain the peak thrust, one assumes that the throat is unblocked and that the body acceleration is the same as when the body is blocking the throat. Results from Ref. 2 show that the body is still accelerating rapidly in a region just downstream of the throat. Therefore, the first term inside the parentheses in Eq. (14) is unity and the second term is the same as before. The resulting peak nondimensional thrust is 1.18. After this point is reached, the body acceleration term drops quickly to zero and the relationship in Eq. (12) holds. The resulting thrust model is presented in Fig. 14.

When the thrust history of Fig. 14 is used as a forcing function to the test stand, the agreement between the thrust model and the test data can be ascertained. The test stand natural frequency and damping were estimated from the test data. Figure 15 compares the results of the calculation with the test data. It shows a fair agreement between the curves, which indicates that the assumption of constant blockage will give a reasonable thrust prediction if high resolution pressure data are available. The blockage and decay analysis presented should be adequate for distinguishing a mass ejection from a burn area phenomenon.

Unexpected Increase in Burn Rate

To this point, anomalies resulting from an unexpected change in throat area (due to mass ejection) or burn surface area have been described. Another factor that could conceivably cause a pressure disturbance would be a burn rate excursion not explained by the normal cP^n relationship.

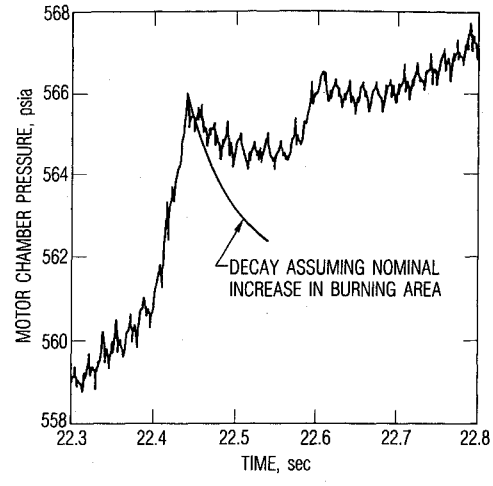

Fig. 16 IUS SRM-2 pressure disturbance.

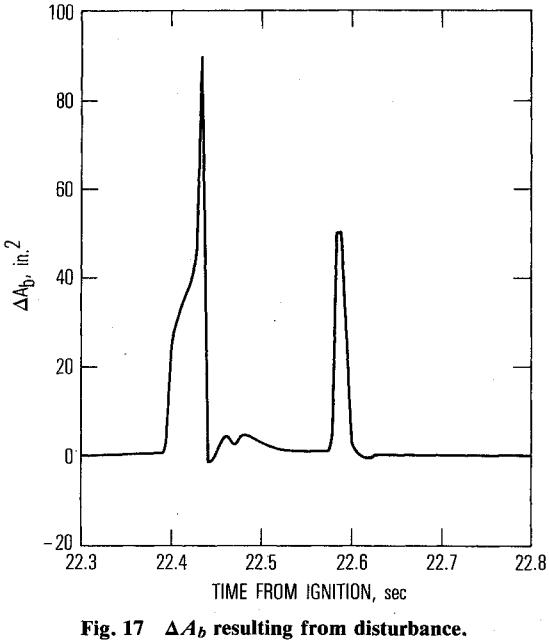

Fig. 17 ΔA_b resulting from disturbance.

It is known that low density propellant such as porous propellant can cause large burn rate variations and even lead to propellant detonations under some circumstances (see Ref. 4). In addition, local variations in propellant oxidizer concentration lead to localized high burn rate regions within the grain. Incomplete mixing of the fine ground ammonium perchlorate (AP) used in many propellants results in pockets of AP-rich propellant with enhanced burning characteristics. Local variations in burn rate catalysts such as ferric oxide or N-Butyl Ferrocene could also cause burn rate enhancements. Unfortunately, very little data exist to help quantify the level of enhancement that could be observed due to local variations in propellant composition. One would have to envision a pressure anomaly caused by this mechanism to be small since propellants must be well mixed to achieve uniform ballistic and physical properties, i.e., any pockets of nonuniform propellant should be small.

Figure 16 presents the pressure for two disturbances that occurred on a static test of the IUS SRM-2 motor. Officials at Arnold Engineering Development Center noted that similar disturbances have been experienced on several of the rocket motor test programs that utilized that facility. Mass ejection (for the first disturbance) would require a throat area decrease of 10%, i.e., an object 1.3 in. in diameter and about 2 ft long, then tapering to zero, to explain the decay. Therefore, mass

ejection was ruled out. The anomaly was analyzed as a burn area increase giving the result shown in Fig. 17. A ΔA_b of 90 in.^{2} would require an unbond 1.2 in. deep or a crack of about 0.6 in. for 360 deg. Neither would decay immediately nor can either be considered likely. Therefore, unbonds and cracks were eliminated.

Voids are a possibility. However, the advent of pressure curing has virtually removed the problem of propellant voids in today's SRMs. The size of voids is generally independent of the size of the motor; therefore, voids will be more of a concern for very small motors than for larger motors. Analysis of a disturbance in terms of voids is very difficult since the shape, number of voids, and spacing between voids are all unknowns. However, calculation of a ΔA_b vs time curve for a disturbance could allow simple estimates of void size. For the peak ΔA_b in each of the spikes, one can calculate the equivalent diameter of a spherical void with this surface area, which results in a diameter of 5.4 and 4.0 in. for the first and second spike, respectively. Even if one postulates 100 spherical voids of equal diameter, the diameters would have to be 0.54 and 0.4 in. for the two spikes. Since even voids of this size would be revealed by x-ray inspections, the likelihood of voids causing the disturbance is small. In addition, voids of this size would disrupt the ensuing surface area-web history, a phenomenon that was not observed on this particular test. One can postulate a larger number of smaller voids that would not disturb subsequent events. The total area of voids is independent of their diameter if it is assumed they lie in a single plane. The phenomena of Fig. 16 is not an isolated event and if the cause is voids, it is surprising that they always occur in a plane of the burn surface so as not to disturb subsequent events. Therefore, voids were eliminated as a possible cause.

A propellant burn rate anomaly was the only mechanism that had not been eliminated. To investigate this possibility, an estimate was made of the propellant burned to achieve each ΔA_b. The integration results in propellant weight estimates of 0.017 and 0.006 lb for the first and second spikes, respectively. These propellant weights correspond to volumes of 0.27 and 0.09 in.^{3} for a propellant density of 0.0635 lb/in.^{3}. Therefore, the actual volume of propellant is very small. The disturbance can be explained if one assumes the pocket burns at explosive or even near detonation velocities.[4] The larger pocket would have a diameter of 0.8 in., and the rapid combustion would result in a small void that would not cause any noticeable change in the following surface areas.

In practice, one could assume that almost any disturbance could be generated by enhanced burn rate propellant because the enhancement factor and anomalous propellant volume geometry are not known. For this reason, mass ejection and burning surface area increases should be investigated prior to burn rate anomalies. It is realistic to assume that burn rate anomalies cause only small disturbances since proper mixing results in a nearly homogeneous propellant.

Conclusions

Proper analysis of ballistic anomalies can aid in uncovering motor design deficiencies or unique motor characteristics. The three principal causes for ballistic anomalies are an unexpected increase in burning surface, mass ejection, and pockets of high burn rate propellant. Solution of the mass and energy balance equations within the motor shows that chamber temperature variations may be neglected.

Analysis of cracks and debonds show that these phenomena generally decay over much longer periods of time than disturbances caused by mass ejection. Debond or crack decay time is proportional to the angle between the additional exposed surface and the burn front. Analyses of a debond occurring on a Titan SRB showed the relative magnitude of the disturbance and that the debond had to propagate with time.

Events associated with mass ejection have very short rise times (of the order of a few milliseconds) and should decay within three to four motor time constants. For motors with moderate to large port-to-throat ratios, a thrust decrease will be realized while the body is in the throat region. Analysis of a mass ejection during the IUS DL-1 test shows that the theoretical pressure decay curve closely matches the decay observed during an actual ejection. High resolution pressure data are necessary in order to calculate the amount of blockage and the resultant thrust history. Thrust calculated from pressure data on the DL-1 firing agrees well with measurements from the test.

Incomplete mixing of propellant could lead to small regions that have higher burn rates than homogeneous propellant. Small pockets of high burn rate propellant burn out rapidly and would not particularly affect the subsequent burnback.

Acknowledgment

This study was supported by the Space Division Air Force Systems Command under Contract F04701-83-C-0084.

References

[1]Krier, H., "Solid Propellant Burning Rate During a Pressure Transient," *Combustion Science and Technology*, Vol. 5, 1972, pp. 69–73.

[2]Murdock, J. W., "Rocket Thrust Perturbation Caused from Discharge of an Inert Body," *Journal of Propulsion and Power*, Vol. 2, No. 2, 1986, pp. 117–123.

[3]Landsbaum, E. M., "The Effect of a Shock Wave on a Burning Solid Propellant," *Advances in Aeronautical Sciences*, Vols. 3–4, Pergamon, New York, 1961, pp. 497–511.

[4]Kuo, K. K., Vichnevetsky, R., and Summerfield, M., "Theory of Flame Front Propagation in Porous Propellant Charges Under Confinement," *AIAA Journal*, Vol. 11, No. 4, 1973, pp. 444–451.